Experimental study on the evolution of 3D surface flaws under true triaxial stress state

Wu, Zhuorui; Wang, Jie; Deng, Shuxin; Wang, Zhen; Zhou, Yubao; Deng, Bozhi

DOI
10.1016/j.cscm.2025.e04827

Publication date
2025

Document Version
Final published version

Published in
Case Studies in Construction Materials

Citation (APA)
Wu, Z., Wang, J., Deng, S., Wang, Z., Zhou, Y., & Deng, B. (2025). Experimental study on the evolution of 3D surface flaws under true triaxial stress state. *Case Studies in Construction Materials*, *22*, Article e04827. https://doi.org/10.1016/j.cscm.2025.e04827

Case Studies in Construction Materials 22 (2025) e04827

Contents lists available at ScienceDirect

Case Studies in Construction Materials

journal homepage: www.elsevier.com/locate/cscm

Experimental study on the evolution of 3D surface flaws under true triaxial stress state

Zhuorui Wu [a,b], Jie Wang [c], Shuxin Deng [a], Zhen Wang [c], Yubao Zhou [d,*], Bozhi Deng [e]

[a] *School of Safety science and engineering, Nanjing University of Science and Technology, Nanjing 210094, China*
[b] *State Key Laboratory of Intelligent Construction and Healthy Operation and Maintenance of Deep Underground Engineering, Xuzhou, China*
[c] *School of Mechanical Engineering, Nanjing University of Science and Technology, Nanjing 210094, China*
[d] *Faculty of Civil Engineering and Geosciences, Delft University of Technology, Delft 2628CN, the Netherlands*
[e] *School of Resources and Safety Engineering, Chongqing University, Chongqing, China*

ARTICLE INFO

Keywords:
3D surface flaw
Intermediate principal stress
Characteristic stress
Crack patterns
CT scanning

ABSTRACT

The true triaxial stress are typical stress state in the deep underground. 3D surface flaws, one of the most common type of flaws, extensively existed in the rocks. Therefore, the study on evolution of the 3D surface flaw under true triaxial stress is crucial to determine the fracture behaviors of the rock in some deep underground spaces. Gypsum, as a rock-like material, has been extensively used in studies of crack initiation and propagation. In this study, we prefabricate a pair of 3D surface flaws at 45° in the cubic gypsum specimen and investigates the effect of the intermediate principal stress on initiation and peak stresses (characteristic stress thresholds) of flaws and crack propagation patterns of 3D surface flaws parallel to the intermediate principal stress. The true triaxial apparatus and acoustic emission (AE) technique were used to test and monitor the mechanical behaviors of the samples. The internal crack propagation pattern was observed by X-ray CT scan. The results demonstrate that the intermediate principal stress strongly affects crack patterns but has a limited influence on characteristic stress thresholds. Both the intermediate and minimum principal stresses affect the difference in the crack peak and initiation stress, which elucidates how the true triaxial stress affects the fracture behavior of the specimen. Additionally, the intermediate principal stress effect on characteristic stresses is closely related to the magnitude of minimum principal stress. When the magnitude of minimum principal stress is small, with the rising intermediate principal stress, the characteristic stresses increase slowly. When the magnitude of minimum principal stress is large, the intermediate principal stress almost has no effect on characteristic stresses. The surface wing cracks and anti-wing cracks initiate from the flaw when the magnitude of intermediate principal stress is relatively small. With the intermediate principal stress increasing, the surface crack propagation pattern is shift from tensile crack to shear crack. Through the CT image reconstruction technique, the propagation patterns of the inner tips of single 3D surface flaw were illustrated in this paper. It is observed that the large intermediate principal stress can restrict the crack wrapping and even make the internal flaw propagation patterns same with that on the specimen surface, providing insights into the validity of simplifying 3D flaws as 2D flaws for analyzing and computing crack propagation.

* Corresponding author.
E-mail address: y.zhou-16@tudelft.nl (Y. Zhou).

https://doi.org/10.1016/j.cscm.2025.e04827
Received 2 February 2025; Received in revised form 5 May 2025; Accepted 24 May 2025
Available online 26 May 2025

1. Introduction

As tunnel construction advances into deeper underground environments, accurate prediction of fracture in surrounding rocks under extreme stress conditions is critical to assessment of deep tunnels risks. True triaxial stress, a dominant stress state in deep geomechanical context [1], fundamentally governs rock fracture failure processes. Experimental studies on crack evolution under true triaxial stress can provide mesoscopic insights to elucidate the fracture mechanisms of materials [2–4], which are beneficial to prediction of fracture failure in deep tunnels.

To now, there are many investigations on the evolution of 2D flaws (a kind of flaw which penetrate the whole specimen) embedded in various materials, such as polymethyl methacrylate (PMMA) [2] and sandstone [3], marble [4], gypsum [4,5], under uniaxial compression test [5–8], tension test [9], or biaxial compression test [10–12]. These results demonstrate the effect of flaw angle, geometry and number on the initiation, coalescence and characteristic stress thresholds. Additionally, the observation of crack types can also elucidate the failure type of specimen under different stress state. For example, Wong et al. [3] identified seven types of cracks emanating from one single prefabricated flaw in uniaxial test based on the propagation patterns and mechanism. From now on, flaws denote the pre-fabricated cracks in the specimens. Yang et al. [13] observed eight types of crack coalescence in two parallel flaw propagation under uniaxial stress. The frictional force along the flaw surfaces can affect the crack evolution under uniaxial loading [5]. In triaxial experiments, the crack types and the mechanical behavior of the specimen are strongly influenced by the confining pressure [14–16]. Large confining pressure will induce obvious plastic deformation and decrease the number of new cracks [17,18]. Furthermore, previous studies on 2D through-cracks have revealed the mechanisms of the effect of the intermediate principal stress on crack propagation and stress thresholds [19,20].

In fact, among natural rock flaws, 3D flaws are ubiquitous in rocks and play a pivotal role in fracture propagation [21,22]. Therefore, understanding the evolution of 3D flaws under true triaxial stress is essential for prediction of the rock fracture behavior in deep underground spaces [20]. To observe the patterns of 3D flaws in the internal of specimens, the CT scan technique was employed to visualize internal crack patterns after the experiment was completed [23,24]. Additionally, the acoustic emission (AE) technique is an effective method to monitor the cracking process and obtain the crack initiation stress [25,26]. The accuracy of AE method has been verified [27]. These techniques are beneficial to observation and monitor of 3D internal fracture patterns.

Some experiments demonstrated the uniqueness of the propagation process of 3D cracks under uniaxial or biaxial compression test [28,29], which is different with that of 2D flaws [24,30]. For example, in uniaxial loading tests on 3D flaws, the wing wrapping crack can be observed in the tips of the 3D flaws [31]. And wrapping cracks constrain themselves to further propagate [29]. The resulting crack surfaces are non-planar and typically consist of a combination of shear and tensile cracks [32]. While under biaxial stress state, Wang et al. [33] investigates the restriction effect of lateral stress on the wrapping crack growth of the 3D internal flaw embedded in the resin samples. It is observed that the relative high lateral stress can restrict the generation of wrapping cracks.

In deep underground environments, the in-situ stress state are typically three unequal principal stresses (true triaxial stress) [1]. It is necessary to investigate the 3D flaw propagation under this stress state. Sun et al. [34] conducted a numerical study on the effect of true triaxial stress on 3D crack propagation and demonstrated that σ_2 significantly influence crack initiation stress. However, this study did not validate its numerical models which requires experiments on real 3D flaw. This is the necessity of our study. Some studies demonstrate that the anisotropic lateral stresses ($\sigma_2 \neq \sigma_3$) fundamentally affect the fracture process [35–37]. However, they predominantly focused on the macroscopic effect of σ_2 on fractures, while its effect on 3D surface flaws evolution remains inadequately studied. This knowledge gap impedes a mechanistic understanding of how σ_2 affects crack initiation and propagation at mesoscopic scales. Therefore, experimental investigation on 3D surface flaws propagation under true triaxial stress loading can provide valuable insights into the mesoscale fracture mechanisms governing rock fracture failure processes [38] and advance predictive capabilities for rock damage in deep underground tunnels [17].

In Section 1, we review the up-to-date literatures on the flaw evolution. In Section 2, we detail the true triaxial experimental methods and fabrication process of 3D surface flaws in specimens. Sections 3 and 4 describe the results of the experiments from two aspects, one is characteristic stress thresholds, the other is cracks patterns affected by the minimum and intermediate principal stresses. Then we compare the results with other previous studies. Finally, we conclude the experiment observation in the Section 5 and 6.

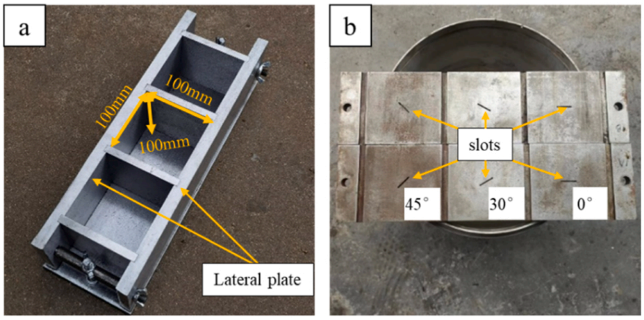

Fig. 1. (a)The designed mold and (b)lateral slots at various inclinations.

2. Experiment setup

2.1. Apparatus

To fabricate 3D surface flaws embedded in the specimens, we designed a stainless mold (see Fig. 1) featuring three pairs of slots at various angles on the lateral plates. which can prefabricate multiple types of flaws by inserting different materials. For example, inserting plastic thin films can make closed flaws, while inserting steel sheets of varying geometries can make opened flaws or 3D surface flaws. The mold is capable of fabricating three specimens with different inclination angles simultaneously. The dimension of specimens is of 100 × 100 × 100 mm.

The experimental apparatus used in this study is custom-designed and fabricated to apply true triaxial stress using six independently controlled loading platens (see Fig. 2). The system consists of six loading actuators and a high-stiffness loading frame, with a maximum loading capacity of 600 MPa along the X and Y axes and 400 MPa along the Z axis. To minimize friction, a mixture of Vaseline and stearic acid was applied to all surfaces of the specimens and platens. Furthermore, the specimens were coated with copper foil, reducing the coefficient of friction to approximately 0.02 [35].

Additionally, the end friction effect caused by platen friction has been extensively studied by Feng et al. [35]. Their findings demonstrate that it can increase stress in orthogonal directions, particularly in the minimum principal stress direction.

2.2. Specimen

Cement-based rock-like materials (e.g., gypsum and concrete) are widely adopted in fracture mechanics experiments as analogues for natural rocks due to their comparable mechanical properties [4]. Their controlled casting process enables precise prefabrication of 3D surface flaws with tailored geometries – a critical advantage over natural heterogeneous rocks. Notably, gypsum has been extensively validated through prior studies investigating crack propagation patterns, providing established benchmarks for experimental comparisons. Given its reproducibility, ease of flaw customization, and empirical verification, gypsum emerges as an ideal model material for fracture analysis. In this study, the specimens were prepared using ultra-high strength gypsum powder mixed with purified water at a mass ratio of 100:26. Water should be added to the blender first, followed by the gradual addition of gypsum powder, ensuring thorough mixing. Then the gypsum paste should be vibrated to expel internal air before casting.

To make pre-existing 3D flaws within the specimens, two 0.3 mm thick stainless steel sheets were used, with one end cut into a 100 mm radius arc. The sheets were symmetrically inserted into the mold slots on both sides to a depth of 25 mm, and rubber strips were used to seal the slots to prevent paste leakage and restrict the movement of the steel sheet. Vaseline was applied to the steel sheets to facilitate removal of the sheets after paste solidification. As shown in Fig. 3, the finished specimens containing the flaws that are oriented at a 45-degree angle and parallel to the intermediate principal stress direction. The prefabricated 3D flaws feature both inner arc tips and outer tips, representing a combination of 3D and 2D flaw characteristics.

The gypsum specimens were maintained in a thermostat-controlled container to enhance their brittleness. It is important to note that the temperature of the container was carefully regulated to remain below 65°C to prevent dehydration at the molecular level of the gypsum. Subsequently, the surfaces of the specimens were mechanically polished to ensure smoothness and minimize frictional effects.

Each step of the sample processing procedure was meticulously executed to ensure maximum consistency across all specimens. To validate the quality and uniformity of the processed samples, three randomly selected specimens were tested, and the standard deviation as well as the coefficient of variation of the data were analyzed. The results (Table 1) indicated that the properties of the three samples were highly consistent, confirming the high quality and uniformity of the specimens.

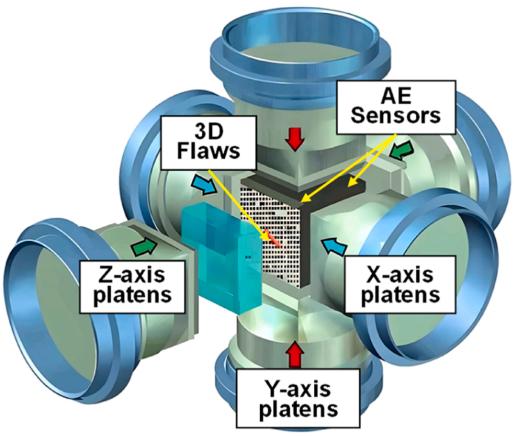

Fig. 2. Schematic of true triaxial loading structure.

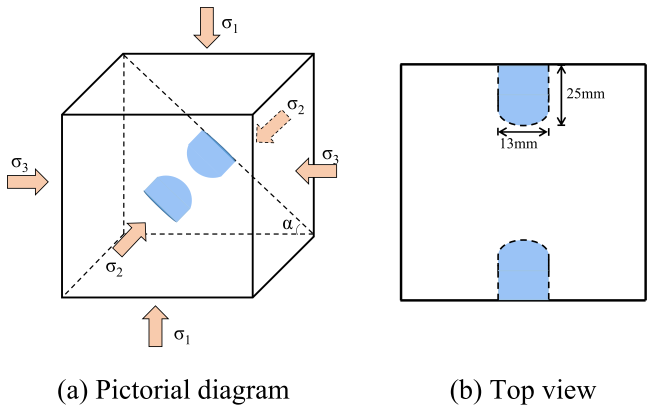

Fig. 3. Schematic of a specimen with a 45-degree 3D surface crack.

Table 1
Physical properties of gypsum specimen.

Properties	Average value	Standard deviation	Coefficient of variation
Porosity	9.67 %	0.01	0.12
Density, ρ	1.95 g/cm^3	0.03	0.02
Young's modulus, E	6.76 GPa	0.42	0.06
UCS, σ_c	33.2 MPa	1.90	0.06
UTS, σ_t	4.66 MPa	0.16	0.04
Poisson's ratio, ν	0.16	0.01	0.07

2.3. *Experiment method*

In this study, σ_1, σ_2, and σ_3 represent the maximum, intermediate, and minimum principal stresses, respectively. Given the critical role of σ_2 in true triaxial tests, we primarily focus on the evolution of 3D surface flaws aligned with the direction of σ_2 to elucidate its underlying mechanisms.

The true triaxial stress path is illustrated in Fig. 4. Firstly, we rise the three principal stresses synchronously to σ_3 value at the rate of 0.1 MPa/s. Then one of three principal stresses is held constant while the other two principal stresses are both increased to σ_2 values. The final step is regulating the strain rate at 0.001 mm/s until σ_1 reaches the point of specimen failure. There is a 15 s interval between steps ensuring stress stable. The specimens are tested based on the scheme outlined in Table 2.

The crack initiation stress (σ_i) and peak stress (σ_p) are two significant stress thresholds to characterize the crack initiation and specimen failure, respectively. The linear acoustic emission (AE) hit line method is used to identify the crack initiation stress. The schematic of this method is illustrated in Fig. 5, the first sharp increase in AE counts denotes the onset of crack initiation. The loading curve, as shown in Fig. 5, is used to determine peak stress.

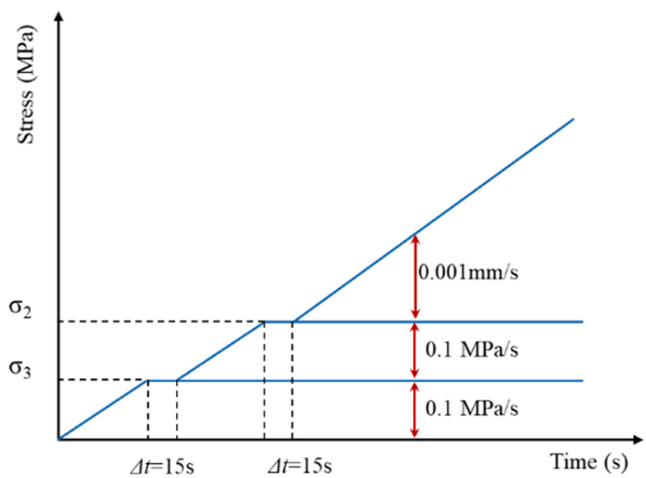

Fig. 4. Schematic of typical true triaxial loading path.

Table 2
Stress paths and results of 3D flaw experiments.

Specimen No.	σ_3 (MPa)	σ_2 (MPa)	σ_i (MPa)	σ_p (MPa)
2T–45–36	10	10	42.2	53.3
2T–45–37		20	42.6	55.2
2T–45–38		30	45.1	55.8
2T–45–39		40	47.5	56.5
2T–45–40		50	47.9	54.5
2T–45–41	20	20	58.2	68.8
2T–45–42		30	64.3	72.2
2T–45–43		40	63.1	74.7
2T–45–44		50	64.4	75.6
2T–45–45		60	65.2	76.1
2T–45–46	30	30	68.7	83.5
2T–45–47		40	69.2	84.3
2T–45–48		50	68.9	85.3
2T–45–49		60	69.5	86.5
2T–45–50		70	70.4	85.9

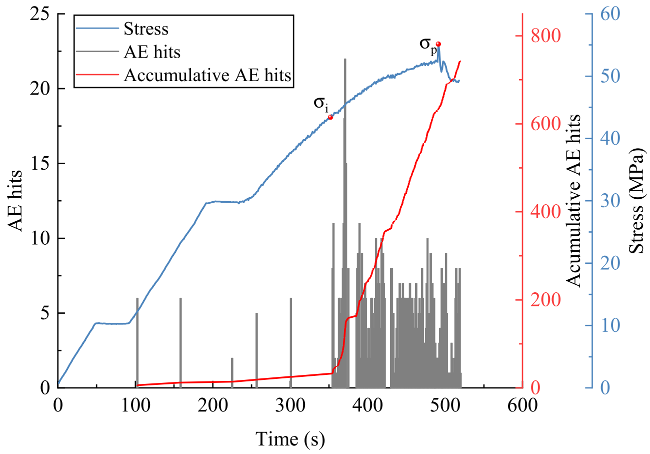

Fig. 5. Schematic of the method to identify the crack initiation and peak stress based on the linear AE hit line method.

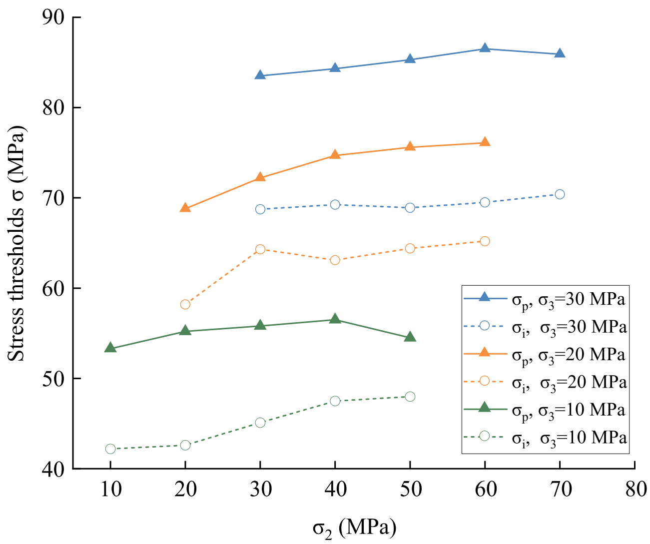

Fig. 6. Effect of σ_2 on the initiation and peak stress of 3D flaws.

The acoustic emission (AE) signal-based method proves more effective for identifying crack initiation compared to classical methods [39]. Zhao et al. [27] proposed and validated the linear AE hit line method to to determine initiation stress, demonstrating its reliability through experimental verification.

3. Effect of true triaxial stress on 3D flaw evolution

3.1. Effect of intermediate principal stress

As illustrated in Fig. 6, the initiation stress generally shows a slight increase with rising σ_2. This trend can be attributed to the location and geometry of the 3D surface flaws. In this study, the internal tips of the 3D flaws are positioned close to the specimen surface, resulting in a more uniform stress distribution compared to through-flaw embedded in specimens. Consequently, the influence of σ_2 becomes more pronounced under these conditions. However, when σ_2 exceeds a critical threshold, the initiation and peak stresses begin to decrease.

When σ_3 is low (10 MPa), the initiation stress shows a more pronounced increase with rising σ_2 compared to cases with higher σ_3 values. Although the increasing trend in peak stress gradually diminishes, it still reaches a maximum increase of approximately 5 %. The peak stress initially rises and then decreases as σ_2 increases. When σ_3 is increased to 20 MPa, both the initiation and peak stresses show an upward trend with rising σ_2. Further increasing σ_3 to 30 MPa results in higher crack initiation and peak stresses compared to the $\sigma_3 = 20$ MPa group. However, the influence of σ_2 on the characteristic stresses of the flaws becomes significantly weaker. The initiation stress shows minor fluctuations, while the peak stress initially increases and subsequently decreases as σ_2 rises.

In summary, the influence of σ_2 on cracking stress thresholds is closely related to σ_3. When σ_3 is relatively low, the effect of σ_2 is more pronounced. As σ_3 increases progressively, the influence of σ_2 on cracking stress thresholds diminishes. This phenomenon can be attributed to the end friction in the σ_2 direction, which affects crack propagation. When σ_3 is low, the strain in the σ_3 direction is larger, resulting in greater friction at the end of the σ_2 direction. This indirectly increases the "pseudo" σ_3, thereby restricting crack propagation and leading to significant increases in both initiation and peak stresses. As σ_3 rises, the confining effect of σ_3 on deformation in its own direction becomes more pronounced, causing the end friction in the σ_2 direction to weaken.

As illustrated in Fig. 7, the macroscopic deformation behavior of specimens containing 3D surface flaws can be characterized as a combination of behaviors observed in specimens containing opened cracks and closed cracks. Prior to reaching peak stress, the load-displacement curve remains relatively smooth, resembling that of specimens containing open cracks. It is attributed to the absence of frictional forces at the flaw surfaces, resulting in minimal stress fluctuations. However, as σ_1 continues to increase, a significant stress drop occurs at peak stress, followed by a subsequent stress recovery that even exceeds the last peak stress. In this case, the strain curves exhibit characteristics similar to those of specimens containing closed cracks. At the point of stress drop, crack surfaces begin to make contact, generating substantial frictional forces that resist further shear slip. This frictional resistance enhances the specimen strength.

3.2. Effect of minimum principal stress

The influence of σ_3 on crack propagation is clearly demonstrated in Fig. 8. An increase in σ_3 leads to a significant rise in both initiation and peak stresses, highlighting its restraining effect on crack propagation. Figs. 8 and 9 further illustrate the relationship

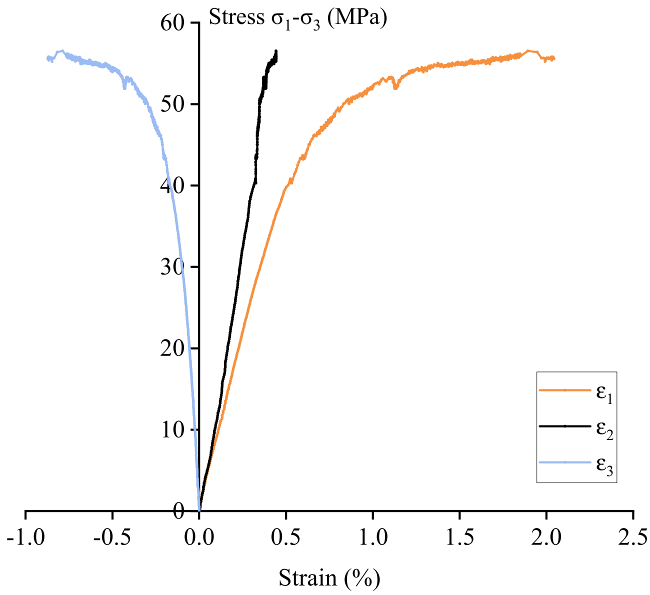

Fig. 7. The stress strain curve of the specimen containing 3D surface flaws (σ_3=10 MPa , σ_2=50 MPa).

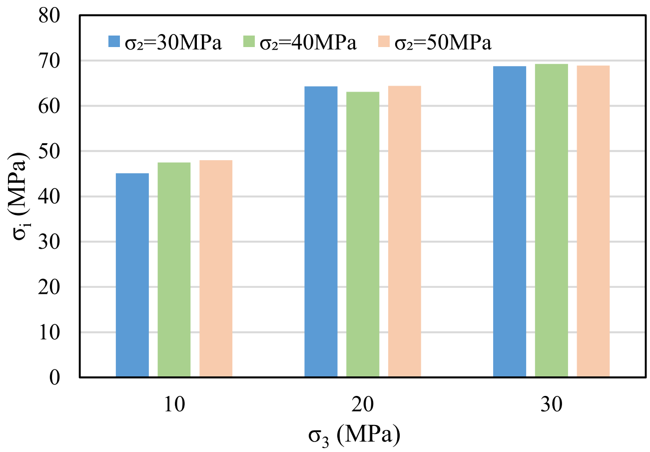

Fig. 8. Effect of σ_3 on crack initiation stress.

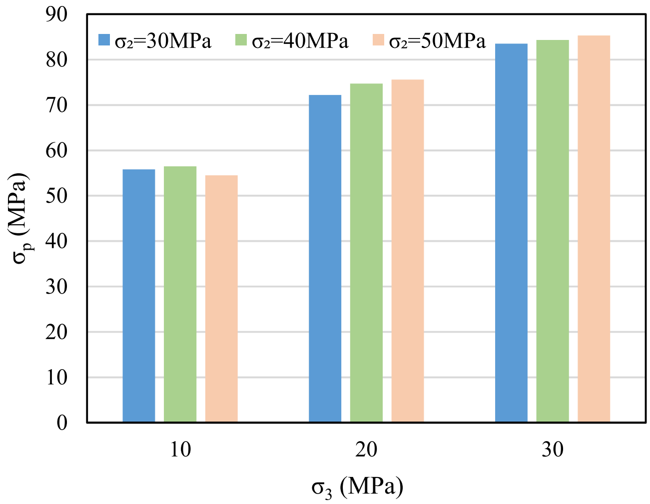

Fig. 9. Effect of σ_3 on crack peak stress.

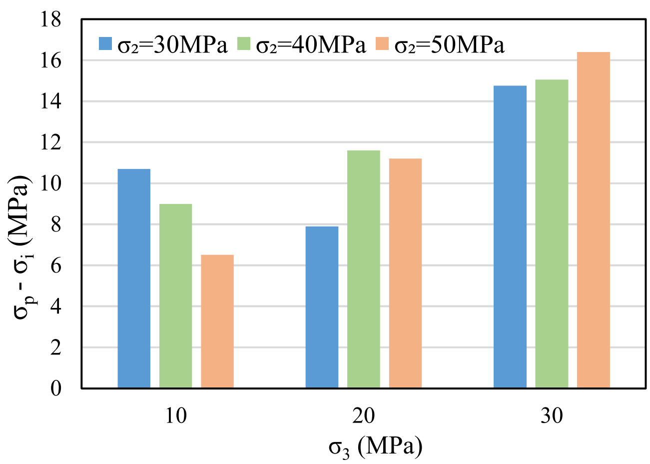

Fig. 10. Effect of σ_3 on difference of characteristic stress.

between σ_3 and characteristic stresses. Specifically, Fig. 8 depicts the effect of σ_3 on characteristic stress using histograms. As σ_3 increases, the average initiation stress rises markedly by approximately 13 MPa (or 30 %). However, when σ_3 increases from 20 MPa to 30 MPa, the rate of increase in crack initiation stress slows down.

Regarding the influence of σ_3 on peak stress, as shown in Fig. 9, the peak stress also increases with rising σ_3. For example, when σ_3 increases from 10 MPa to 20 MPa, the average peak stress rises from 55.6 MPa to 74.2 MPa, representing an increase of approximately 33 %. Further increasing σ_3 to 30 MPa results in an average peak stress of 84.4 MPa, corresponding to an increase of about 14 %. Notably, the rate of increase progressively decrease as σ_3 rises. This phenomenon can be attributed to the intrinsic properties of the gypsum material. Under high confining pressure, the plastic deformation of gypsum becomes more pronounced, significantly influencing the mechanical behavior of the specimens.

The characteristic stress difference, defined as the difference in peak stress and initiation stress, represents the strain-hardening phase between crack initiation and failure. A larger characteristic stress difference indicates a more extensive strain-hardening range. As illustrated in Fig. 10, the stress difference increases with rising σ_3, suggesting that a higher σ_3 extends the strain-hardening phase.

When σ_3 is 10 MPa, the characteristic stress difference decreases as σ_2 increases. However, when σ_3 increases to 20 MPa, the characteristic stress difference initially rises and then decreases with increasing σ_2. As σ_3 further increases to 30 MPa, the characteristic stress difference decreases with rising σ_2. These observations are consistent with rock failure patterns observed in true triaxial tests [40, 41]. Specifically, when σ_3 remains constant, an increase in σ_2 either extends or shortens the elastic region of the stress-strain curve.

This phenomenon can be attributed to the differential stress (σ_2-σ_3). Smaller differential stress (σ_2-σ_3) does not induce the damage during the second step loading. While lager differential stress (σ_2-σ_3) can induce damage in advance, which potentially accelerate the failure of the specimen.

Thus, we deeply analyze of the effect of differential stress (σ_2-σ_3) on the characteristic stress difference, as illustrated in Fig. 11. The results indicate that an increase in the differential stress (σ_2-σ_3) enhances the influence of σ_3 on the difference of characteristic stresses. Larger differential stress (σ_2-σ_3) can accelerate the transition from crack initiation to failure, indicating that both the differential stress (σ_2-σ_3) and σ_3 affect the characteristic stress difference.

It can be inferred that as σ_3 continues to increase, the differential stress (σ_2-σ_3) must further increase to a certain level to observe the decrease of the characteristic stress difference. The σ_3 enhances the plastic deformation behavior. Additionally, in true triaxial rock tests, a sufficiently high σ_3 can prevent the rocks strength from decreasing with increases of σ_2. This result is consistent with the phenomenon in macroscopic true triaxial experiments in which the strength will not decrease when the σ_3 is of high magnitude, no matter how σ_2 changes.

Note that the plastic deformation characteristic of gypsum under high-stress levels may affect the results, indicating the necessity for comparative tests with other materials such as natural rocks for further analysis.

4. 3D flaw propagation patterns

In addition to the characteristic stresses, the complex propagation patterns of 3D flaws also need investigation. Because the evolution of 3D cracks is significantly different from the 2D cracks. Understanding how and to what extent σ_2 influences the evolution of 3D surface flaws is crucial for elucidating the fracture mechanism of specimens under true triaxial stress. Since the position of the 3D surface flaw includes two parts, one is the outer tips on the surfaces of the specimen, the other is the inner tips localized in the internal specimens. This section explores the crack evolution from both surface and internal perspectives.

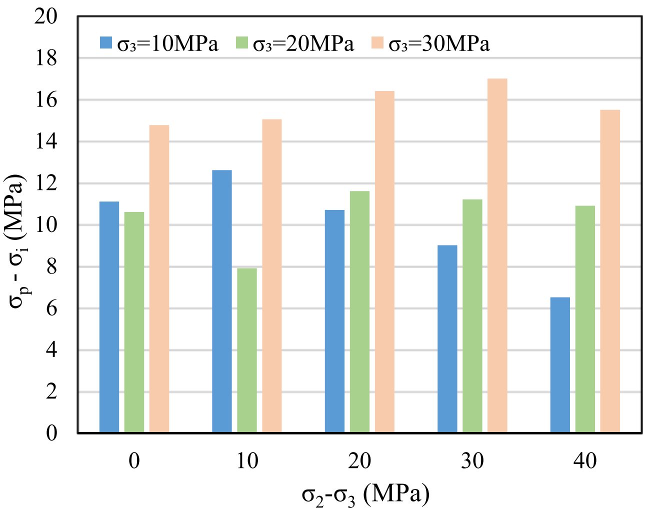

Fig. 11. Effect of differential stress (σ_2-σ_3) on difference in characteristic stresses.

This section provides a detailed analysis of the complex propagation patterns of 3D flaws, as the evolution of 3D cracks differs significantly from that of 2D cracks. Understanding how and to what extent σ_2 influences the evolution of 3D surface flaws is crucial for elucidating the fracture mechanisms of specimens under true triaxial stress. The position of surface 3D flaws includes two parts: the outer tips on the specimen surfaces and the inner tips localized within the specimen. This section explores crack evolution from both surface and internal perspectives.

4.1. Crack propagation patterns on the surfaces

For a σ_3 of 10 MPa, the crack pattern is shown in Fig. 12. As σ_2 increases, the propagation patterns shift from tensile to shear cracks. Specifically, tensile wing cracks and anti-wing cracks initiate from the flaws when σ_2= 10, 20, 30 MPa.

When σ_2 further increases to 40 MPa, both wing cracks and shear cracks initiate from the flaw tips, but the anti-wing cracks do not appear. Finally, when σ_2 reaches 50 MPa, only shear cracks are generated at both tips of the initial flaw, and the anti-wing cracks are only generated at the upper tip of the initial flaw. It reveals that σ_2 can restrain the generation of the anti-wing cracks due to the end friction effect.

Anti-wing cracks commonly occur in the 2D through opened crack propagation experiments. The mechanism behind anti-wing cracks in 3D surface cracks is similar to that in through opened flaws. When the flaw surfaces begin to close and contact due to specimen failure, significant tensile stress occurs at the flaw surfaces and tips, leading to the anti-wing crack formation. However, the anti-wing cracks are less likely to generate from closed flaws, revealing the distinct differences between opened and closed cracks [20].

When σ_3 increases to 20 MPa, as illustrated in Fig. 13, the crack propagation patterns are similar to that at 10 MPa. For intermediate principal stresses of 20 MPa and 30 MPa, both wing and anti-wing cracks initiate from the flaws tips. As the intermediate principal stress further increases to 40 MPa and 50 MPa, anti-wing cracks only initiate from one tip of the flaws. When σ_2 is 60 MPa, only shear cracks initiate from the flaws tips, and anti-wing cracks do not appear.

Both groups of figures reveal that as σ_2 increases, crack propagation will transition from tensile wing cracks to shear cracks. The initiation angle of wing cracks decreased and gradually transitioned to shear cracks. Potentially it is related to “pseudo” σ_3 induced by end friction in the direction of σ_2. This trend indicates the non-negligible effect of σ_2 on crack propagation pattern.

4.2. Crack propagation patterns in the specimens

Given that the propagation of 3D flaws typically involves a wrapping process under uniaxial compression, internal crack propagation generally differs from surface observations. This section is based on CT scan results to analyze the internal crack propagation patterns and illustrate the effect of σ_2. As shown in Fig. 14, the flaw in each specimen was aligned parallel to the X-axis, and the CT scans intersected the samples along the YZ plane. The voxel resolution of the X-ray CT scans is 0.6 × 0.6 × 0.6 mm.

As shown in Fig. 15, when σ_2 = 20 MPa and σ_3 = 10 MPa, the internal crack paths gradually diverge from the outer surface crack paths, demonstrating that the propagation of 3D flaws transitions from the outer to the inner regions. This phenomenon is also known as wing crack wrapping. The internal cracks are shear cracks with an inclination of approximately 60 degrees, which differ significantly from the cracks observed on the surfaces.

We also employed the CT 3D reconstruction technique to reconstruct the structure of the specimens. Light gray represents the matrix of the sample, while dark gray indicates the detected cracks. Cracks with an opening degree exceeding the resolution of the CT apparatus are detected and illustrated in Fig. 16. The results clearly demonstrate that the inner crack patterns consist of wrapping wing cracks mixed with shear cracks, which differ slightly from the outer crack patterns.

As shown in Figs. 17 and 18, when σ_2 increases to 30 MPa and σ_3 remains at 10 MPa, the internal cracks exhibit slight wrapping and gradually align more closely with the surface crack patterns. This indicates that σ_2 significantly influences internal crack propagation. The results confirm that, under high σ_2, internal cracks tend to resemble surface crack paths (see Fig. 18).

As shown in Figs. 19 and 20, when σ_3 = 20 MPa and σ_2 = 20 MPa, the number of internal cracks significantly decreases, and they are tightly closed, making them difficult to detect by CT scanning due to the resolution limitations of the equipment. Even anti-wing cracks, which typically result from impact, cannot be observed under these conditions.

As shown in Figs. 21 and 22, when σ_3 = 20 MPa and σ_2 = 30 MPa, the number of internal cracks further decreases. However, σ_2 induces the formation of internal anti-wing cracks. The propagation of anti-wing cracks is more pronounced than that of wing cracks, further underscoring the influence of sudden impact forces on crack propagation. These results also highlight the differences between open flaws and closed flaws. In the case of closed flaws, the crack surfaces are in close contact with each other and may not slip until failure. As a result, impact forces cannot occur, making it difficult to observe anti-wing cracks initiating from closed flaws.

When σ_2 increases to 40 MPa, as illustrated in Figs. 23 and 24, the overall cracks close tightly, making it challenging to observe crack propagation both on the specimen surfaces and internally. An interesting finding from the CT scan results is the presence of small horizontal cracks near the surface that are not visible in surface photographs. This occurs because the anti-friction agent applied before loading has infiltrated these cracks, and its color closely matches that of the gypsum, rendering small surface cracks difficult to detect with the unaided eye. Given that tensile stress is commonly present on crack surfaces during closure, tensile failure-induced anti-wing cracks can occur at any point along the flaw surfaces.

In summary, this section describes the observation of internal cracks using X-ray CT scanning technology. Under low intermediate principal stress (σ_2), 3D surface cracks exhibit spatially complex propagation patterns, with internal crack angles significantly differing from those on the surface. However, as σ_2 increases, the wing wrapping cracks become increasingly constrained, causing internal crack propagation to align more closely with the surface crack pattern. Ultimately, this results in the formation of a macroscopic fracture

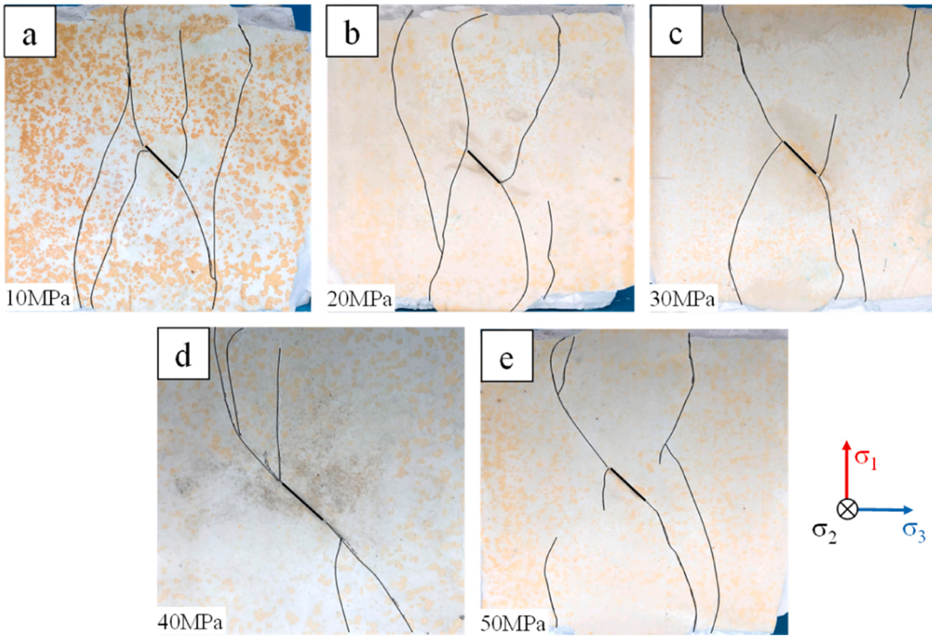

Fig. 12. 3D crack propagation pattern at σ_3= 10 MPa.

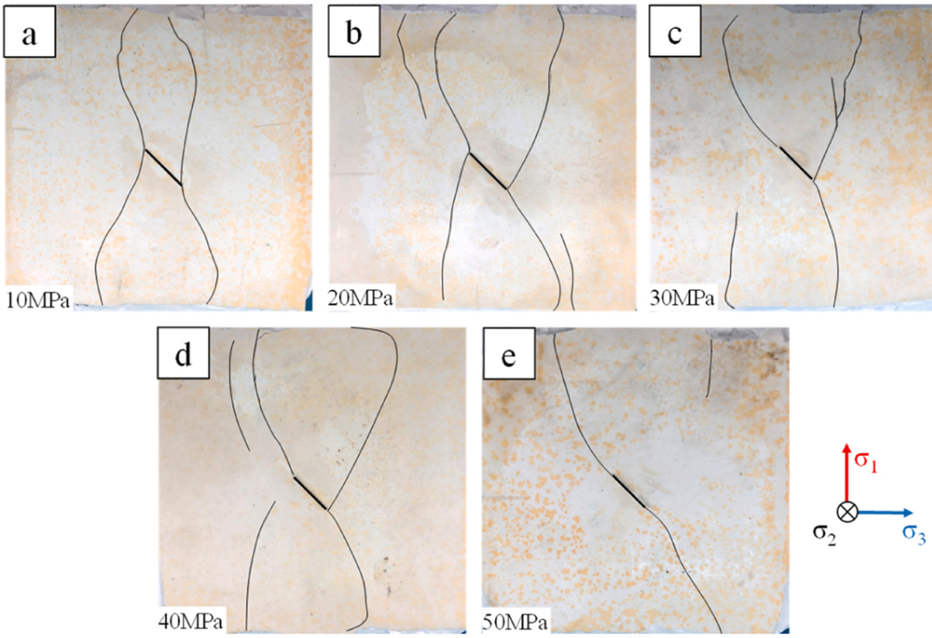

Fig. 13. 3D crack propagation pattern at σ_3= 20 MPa.

zone.

5. Discussion

The evolution of 3D surface cracks is crucial for elucidating the mechanisms of fracture failure. In this paper, we further investigate the evolution of 3D surface cracks under true triaxial stress. The results differ significantly from those observed in uniaxial tests. In uniaxial tests, wrapping wing cracks are commonly observed during loading, which tend to restrict crack propagation [28,29]. However, under true triaxial stress, the wrapping wing cracks gradually diminish as σ_2 increases. This finding is significant as it

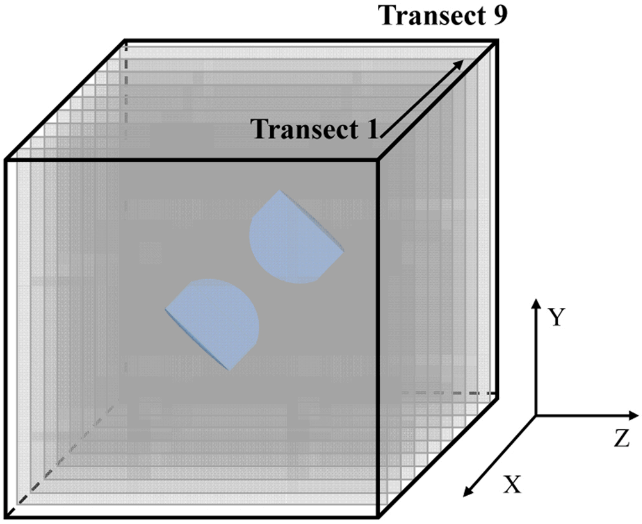

Fig. 14. CT images taken from the section along the YZ plane.

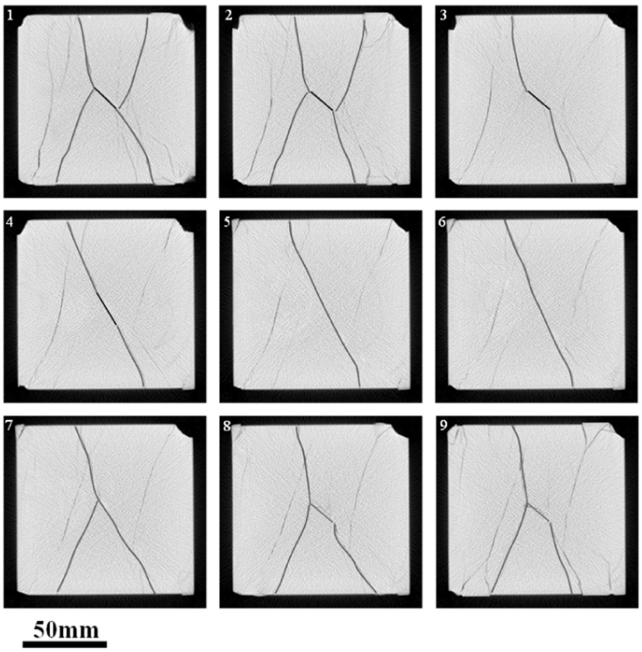

Fig. 15. CT scan of 3D crack (σ_3=10 MPa, σ_2=20 MPa).

validates the method of simplifying 3D crack propagation as 2D crack in numerical computations.

Under such complex stress states, crack propagation mechanisms may exhibit greater intricacy compared to biaxial or uniaxial loading scenarios. Fracture toughness (K_{IC}), a material property typically measured experimentally under plane strain conditions, quantifies a material's resistance to crack growth. However, in 3D stress fields, the determination of fracture toughness may necessitate accounting for additional factors, such as the contributions of stress intensity factor (SIF) components in all three principal directions and their synergistic interactions driving crack propagation.

A primary consideration is the definition of fracture toughness in 3D crack configurations. Fracture toughness is intrinsically linked to the critical SIF, where crack initiation occurs when the SIF reaches this threshold. For 3D cracks, SIFs encompass three modes: K_I (Mode I, opening), K_{II} (Mode II, in-plane sliding), and K_{III} (Mode III, out-of-plane tearing). While K_{IC} is conventionally measured for Mode I-dominated failures (the most prevalent mode), the analysis of 3D cracks may require a coupled evaluation of all three modes. For instance, in the case of a 3D elliptical crack subjected to uniform far-field stresses, the SIF varies along the crack front. According to Irwin's formulation, the Mode I, II and III SIF for such configurations can be expressed as:

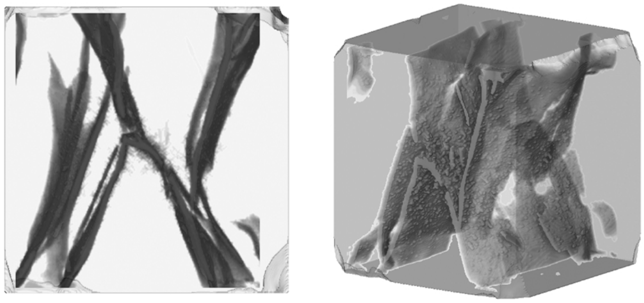

Fig. 16. CT 3D reconstruction image of crack pattern (σ_3=10 MPa, σ_2=20 MPa).

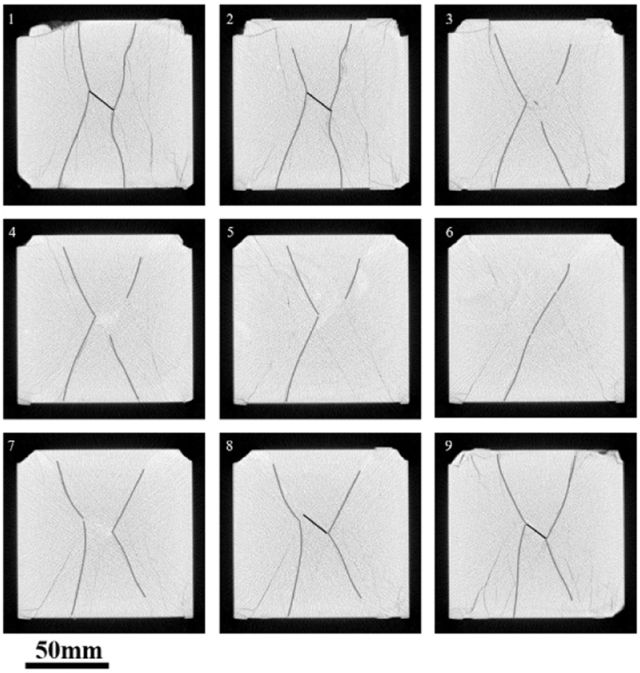

Fig. 17. CT scan of 3D crack (σ_3=10 MPa, σ_2=30 MPa).

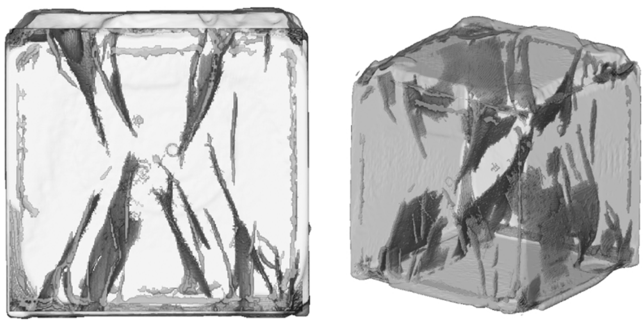

Fig. 18. CT 3D reconstruction image of crack pattern (σ_3=10 MPa, σ_2=30 MPa).

$$K_{IC} = \sigma_{\mathrm{crit}}\sqrt{\pi a} \cdot Y_I \tag{1}$$

$$K_{IIC} = \tau_{\mathrm{crit}}\sqrt{\pi a} \cdot Y_{II} \tag{2}$$

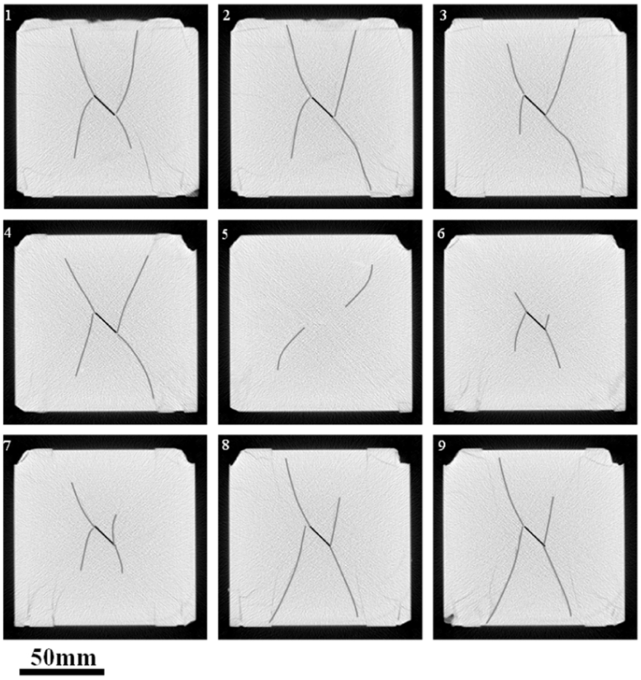

Fig. 19. CT scan of 3D crack (σ_3=20 MPa, σ_2=20 MPa).

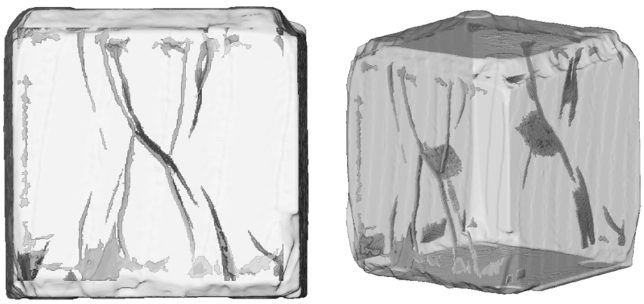

Fig. 20. CT 3D reconstruction image of crack pattern (σ_3=20 MPa, σ_2=20 MPa).

$$K_{IIIC} = \tau_{\text{crit}}^{\text{III}}\sqrt{\pi a} \cdot Y_{III} \tag{3}$$

In which, σ_{crit},$\tau_{\text{crit}}$and$\tau_{\text{crit}}^{\text{III}}$ are critical far-field tensile stress, critical in-plane shear stress, critical out-of-plane shear stress, respectively. And a is crack length (half-length for embedded cracks). Y_I (Mode I), Y_{II} (Mode II), and Y_{III} (Mode III) are geometry-dependent factors for different Mode. The equivalent stress intensity factor can be expressed as:

$$K_{\text{eq}} = \sqrt{K_I^2 + K_{II}^2 + K_{III}^2} \geq K_{IC} \tag{4}$$

The Eq. (4) is obviously difficult for engineering application since it is hard to derive the equivalent stress intensity factor. In fact, based on the results in this study, when the magnitude of σ_2 is relatively large, planar crack propagation dominates, allowing calculations to focus on the σ_1-σ_3 plane (Mode I fracture) while neglecting the influence of σ_2. Take the σ_1-σ_3 plane as an example. In the Eq. (5), σ_x is the stress parallel to the crack plane. σ_y is the stress normal to this plane. This simplification significantly reduces computational complexity.

$$\begin{cases} \sigma_x = \sigma_1 \sin^2\theta + \sigma_3 \cos^2\theta \\ \sigma_y = \sigma_1 \cos^2\theta + \sigma_3 \sin^2\theta \\ \tau_{xy} = \dfrac{1}{2}(\sigma_1 - \sigma_3)\sin 2\theta \end{cases} \tag{5}$$

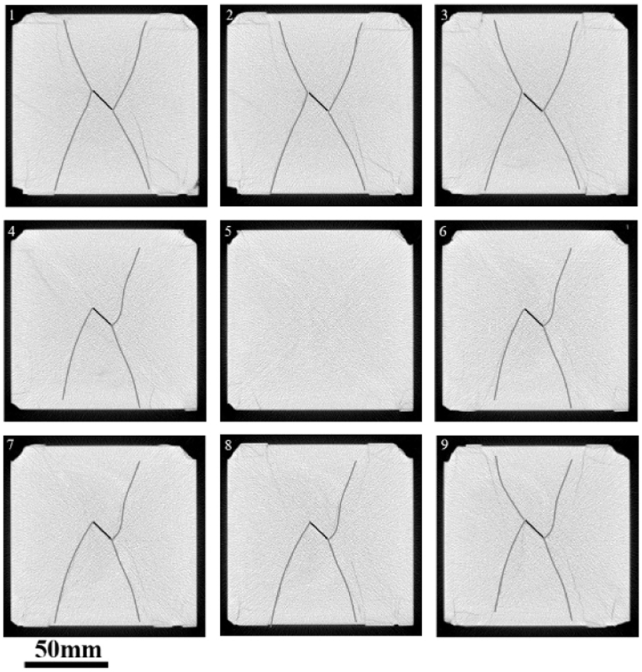

Fig. 21. CT scan of 3D crack (σ_3=20 MPa, σ_2=30 MPa).

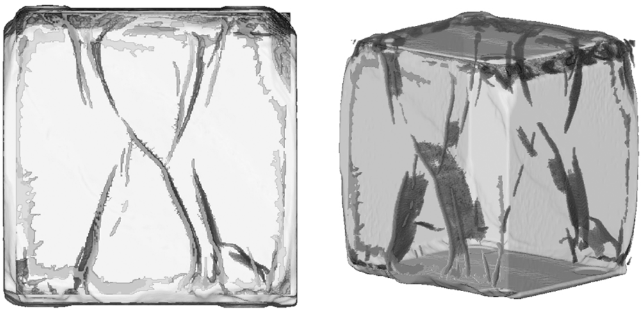

Fig. 22. CT 3D reconstruction image of crack pattern (σ_3=20 MPa, σ_2=30 MPa).

This paper investigates and elucidates the mechanisms of 3D flaw propagation under true triaxial stress states. The results provide insights into the validity of simplifying 3D flaws as 2D flaws for analyzing and computing crack propagation when the magnitude of intermediate principal stress is significant, which helps predict failure modes and validate numerical models. The findings can also contribute to analysis of broader urban maintenance and fracture in building materials.

6. Conclusions

This study investigates the evolution of 3D surface flaws in terms of initiation stress, peak stress, and propagation patterns. The key conclusions are as follows:

Both σ_2 and σ_3 significantly affect the initiation and peak stresses (characteristic stresses) of 3D flaws. As σ_3 increases, the characteristic stresses also increase. However, characteristic stresses initially rise and then decrease with increasing σ_2. An increase in σ_3 increases the difference in peak and initiation stresses, indicating an extended phase from yielding to failure. In contrast, an increase in σ_2 initially increases the difference before decreasing it.

The increase in σ_2 notably influences the propagation patterns of 3D surface flaws. As σ_2 increases, crack propagation transitions from wing cracks to shear cracks, while anti-wing crack propagation gradually diminishes. CT scanning of the specimen interiors reveals that 3D surface flaws exhibit spatially complex cracks (wrapping cracks) under low σ_2 conditions. However, as σ_2 increases, the internal crack patterns align more closely with the surface cracks.

In summary, the results demonstrate the effect of true triaxial stress on the 3D surface flaws evolution, which elucidate the mechanism of 3D surface flaw propagation under true triaxial stress state. Since the fracture failure of rocks is common in deep

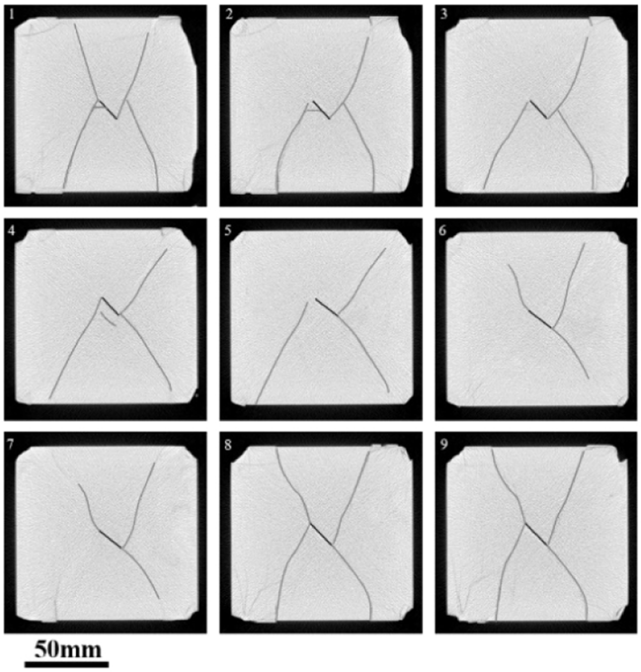

Fig. 23. CT scan of 3D crack (σ_3=20 MPa, σ_2=40 MPa).

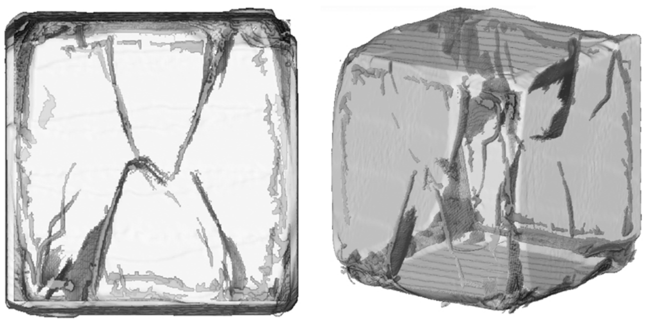

Fig. 24. CT 3D reconstruction image of crack pattern (σ_3=20 MPa, σ_2=40 MPa).

underground tunnel engineering. The results effectively advance predictive capabilities for rock damage in deep underground tunnels—a critical step toward ensuring engineering safety in high-stress geomechanical environments. Besides, the finding of crack patterns in this experimental study provide benchmark datasets for numerical simulations of 3D flaws—a long-standing challenge in computational geomechanics.

CRediT authorship contribution statement

Bozhi Deng: Resources, Funding acquisition, Conceptualization. **Zhuorui Wu:** Writing – original draft, Investigation, Funding acquisition, Conceptualization. **Zhen Wang:** Investigation, Formal analysis. **Yubao Zhou:** Methodology, Formal analysis, Conceptualization. **Jie Wang:** Investigation, Data curation. **Shuxin Deng:** Investigation, Formal analysis.

Declaration of Competing Interest

The authors declare that they have no known competing financial interests or personal relationships that could have appeared to influence the work reported in this paper.

Acknowledgements

The authors are grateful to the funding support by the Jiangsu Funding Program for Excellent Postdoctoral Talent (Grant No.

2023ZB360), State Key Laboratory of Intelligent Construction and Healthy Operation and Maintenance of Deep Underground Engineering (Grant No. SDGZ2513), National Natural Science Foundation of China (Grant No. 52474209). The first author appreciates the help of C.Y Huang, J.Y Wu and X.F Xia in experiments and preparation of specimens.

Data availability

Data will be made available on request.

References

[1] Z. Wu, T. Xu, C. Arson, Effect of the intermediate principal stress on pre-peak damage propagation in hard rock under true triaxial compression, Rock. Mech. Rock. Eng. (2022).
[2] H. Lee, S. Jeon, An experimental and numerical study of fracture coalescence in pre-cracked specimens under uniaxial compression, Int. J. Solids Struct. 48 (2011) 979–999.
[3] L.N.Y. Wong, H.H. Einstein, Systematic evaluation of cracking behavior in specimens containing single flaws under uniaxial compression, Int. J. Rock. Mech. Min. Sci. 46 (2009) 239–249.
[4] L.N.Y. Wong, H.H. Einstein, Crack coalescence in molded gypsum and carrara marble: part 2—microscopic observations and interpretation, Rock. Mech. Rock. Eng. 42 (2009) 513–545.
[5] C.H. Park, A. Bobet, Crack initiation, propagation and coalescence from frictional flaws in uniaxial compression, Eng. Fract. Mech. 77 (2010) 2727–2748.
[6] M. Sagong, A. Bobet, Coalescence of multiple flaws in a rock-model material in uniaxial compression, Int. J. Rock. Mech. Min. Sci. 39 (2002) 229–241.
[7] X.-P. Zhang, L.N.Y. Wong, Cracking processes in rock-like material containing a single flaw under uniaxial compression: a numerical study based on parallel bonded-particle model approach, Rock. Mech. Rock. Eng. 45 (2012) 711–737.
[8] C. Wang, Y. Li, F. Dai, G. Wu, F. Yin, K. Li, K. Wang, Experimental investigation on mechanical properties and failure mechanism of rock-like specimens containing an arc-shaped ice-filled flaw under uniaxial compression, Theor. Appl. Fract. Mech. 119 (2022).
[9] J. Wang, Z. Wu, S. Deng, M. Wang, J. Tao, A. Xie, Z. Wang, The dynamic tensile strength prediction model and tensile behavior of concrete considering pores based on the impact splitting tensile test, J. Build. Eng. 104 (2025) 112272.
[10] A. Bobet, H.H. Einstein, Fracture coalescence in rock-type materials under uniaxial and biaxial compression, Int. J. Rock. Mech. Min. Sci. 35 (1998) 863–888.
[11] E. Sahouryeh, A.V. Dyskin, L.N. Germanovich, Crack growth under biaxial compression, Eng. Fract. Mech. 69 (2002) 2187–2198.
[12] X.P. Zhou, S.L. Peng, J.Z. Zhang, J.N. Zhou, F. Berto, Experimental study on cracking behaviors of coarse and fine sandstone containing two flaws under biaxial compression, Fatigue Fract. Eng. Mater. Struct. (2022).
[13] S.Q. Yang, Y.H. Dai, L.J. Han, Z.Q. Jin, Experimental study on mechanical behavior of brittle marble samples containing different flaws under uniaxial compression, Eng. Fract. Mech. 76 (2009) 1833–1845.
[14] S.Q. Yang, Y.Z. Jiang, W.Y. Xu, X.Q. Chen, Experimental investigation on strength and failure behavior of pre-cracked marble under conventional triaxial compression, Int. J. Solids Struct. 45 (2008) 4796–4819.
[15] D. Huang, D. Gu, C. Yang, R. Huang, G. Fu, Investigation on mechanical behaviors of sandstone with two preexisting flaws under triaxial compression, Rock. Mech. Rock. Eng. 49 (2016) 375–399.
[16] S.-Q. Yang, W.-L. Tian, X.-R. Liu, Y.-H. Huang, J. Yang, An experimental study on failure mechanical behavior and cracking mechanism of rectangular solid sandstone containing two non-coplanar fissures under conventional triaxial compression, Theor. Appl. Fract. Mech. 114 (2021).
[17] W. Jin, C. Arson, Micromechanics based discrete damage model with multiple non-smooth yield surfaces: theoretical formulation, numerical implementation and engineering applications, Int. J. Damage Mech. 27 (2017).
[18] Y. Luo, H. Gong, K. Xu, C. Pei, X. Wei, X. Li, Progressive failure characteristics and energy accumulation of granite with a pre-fabricated fracture during conventional triaxial loading, Theor. Appl. Fract. Mech. 118 (2022).
[19] B. Li, S. Yu, L. Yang, W. Zhu, Y. Xue, D. Feng, C. Wang, Y. Chen, Multiscale fracture characteristics and failure mechanism quantification method of cracked rock under true triaxial compression, Eng. Fract. Mech. 262 (2022).
[20] Z. Wu, Y. Zheng, B. Deng, S. Deng, Influence of intermediate principal stress on rock strength: insights from closed crack evolution under true triaxial compression, Theor. Appl. Fract. Mech. 136 (2025) 104786.
[21] Y. Zhao, C. Chen, S. Wu, P. Guo, B. Li, Effects of 2D&3D nonparallel flaws on failure characteristics of brittle rock-like samples under uniaxial compression: Insights from acoustic emission and DIC monitoring, Theor. Appl. Fract. Mech. (2022) 120.
[22] Y. Zhao, M. Teng, J. Bi, Z. Li, P. Liu, C. Wang, Experimental investigation of fracture behavior of rock-like materials containing 3D embedded flaws subjected to direct and unloading normal stress shear action, Bull. Eng. Geol. Environ. 81 (2022).
[23] M.H.B. Nasseri, F. Rezanezhad, R.P. Young, Analysis of fracture damage zone in anisotropic granitic rock using 3D X-ray CT scanning techniques, Int. J. Fract. 168 (2011) 1–13.
[24] L. Mao, Y. Lei, L. Ding, J. Wu, L. Li, M. Yang, Y. Ju, F.-p Chiang, Evaluation of 3D deformation field in siltstone with a pre-existing 3D surface flaw under uniaxial compression using X-ray computed tomography and digital volumetric speckle photography, Measurement 189 (2022).
[25] X.P. Zhou, J.Z. Zhang, Damage progression and acoustic emission in brittle failure of granite and sandstone, Int. J. Rock. Mech. Min. Sci. 143 (2021).
[26] X.-P. Zhang, G.-G. Lv, Q.-S. Liu, S.-C. Wu, Q. Zhang, P.-Q. Ji, X.-H. Tang, Identifying accurate crack initiation and propagation thresholds in siliceous siltstone and limestone, Rock. Mech. Rock. Eng. 54 (2021) 973–980.
[27] X.G. Zhao, M. Cai, J. Wang, L.K. Ma, Damage stress and acoustic emission characteristics of the Beishan granite, Int. J. Rock. Mech. Min. Sci. 64 (2013) 258–269.
[28] J. Bi, X.P. Zhou, Q.H. Qian, The 3D numerical simulation for the propagation process of multiple pre-existing flaws in rock-like materials subjected to biaxial compressive loads, Rock. Mech. Rock. Eng. 49 (2016) 1611–1627.
[29] T. Zhou, J.B. Zhu, Y. Ju, H.P. Xie, Volumetric fracturing behavior of 3D printed artificial rocks containing single and double 3D internal flaws under static uniaxial compression, Eng. Fract. Mech. 205 (2019) 190–204.
[30] X.-P. Zhou, L. Fu, W. Ju, F. Berto, An experimental study of the mechanical and fracturing behavior in PMMA specimen containing multiple 3D embedded flaws under uniaxial compression, Theor. Appl. Fract. Mech. 101 (2019) 207–216.
[31] Y. Lu, L. Wang, D. Elsworth, Uniaxial strength and failure in sandstone containing a pre-existing 3-D surface flaw, Int. J. Fract. 194 (2015) 59–79.
[32] P. Lin, R.K. Wang, W. Zhou, Q. Yang, The 3D-crack growth mechanism of brittle material under 3D compression, Key Eng. Mater. 353-358 (2007) 1181–1184.
[33] H. Wang, A. Dyskin, E. Pasternak, P. Dight, M. Sarmadivaleh, Effect of the intermediate principal stress on 3-D crack growth, Eng. Fract. Mech. 204 (2018) 404–420.
[34] Y. Sun, F. Fei, L.N.Y. Wong, J. Choo, Intermediate principal stress effects on the 3D cracking behavior of flawed rocks under true triaxial compression, Rock. Mech. Rock. Eng. 57 (2024) 4607–4634.
[35] X.T. Feng, X.W. Zhang, R. Kong, G. Wang, A novel mogi type true triaxial testing apparatus and its use to obtain complete stress-strain curves of hard rocks, Rock. Mech. Rock. Eng. 49 (2016) 1649–1662.
[36] J. Zhang, H. Wang, J. Yu, W. Cai, T. Zhang, Compression-induced failure characteristics of brittle flawed rocks: mechanical confinement-dependency, Theor. Appl. Fract. Mech. 134 (2024) 104678.
[37] B. Haimson, J.W. Rudnicki, The effect of the intermediate principal stress on fault formation and fault angle in siltstone, J. Struct. Geol. 32 (2010) 1701–1711.

[38] Y. Zhang, G. Chen, Z. Wang, D. Liu, Fracture evolution analysis of rock bridges in hard rock with nonparallel joints in true triaxial stress states, Rock. Mech. Rock. Eng. 56 (2023) 997–1023.
[39] G.K. Zhang, H.B. Li, M.Y. Wang, X.F. Li, Crack initiation of granite under uniaxial compression tests: a comparison study, J. Rock. Mech. Geotech. Eng. 12 (2020) 656–666.
[40] R. Kong, X.T. Feng, X.W. Zhang, C.X. Yang, Study on crack initiation and damage stress in sandstone under true triaxial compression, Int. J. Rock. Mech. Min. Sci. 106 (2018) 117–123.
[41] B. Haimson, True triaxial stresses and the brittle fracture of rock, Pure Appl. Geophys. 163 (2006) 1101–1130.